Solar Energy 287 (2025) 113232

Contents lists available at ScienceDirect

Solar Energy

journal homepage: www.elsevier.com/locate/solener

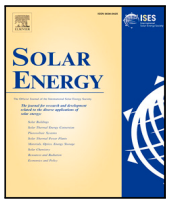

Key parameters influencing wind-induced aeroelastic responses of single-axis solar trackers in photovoltaic plants

Giorgio Frontini, Filippo Calamelli, Sara Muggiasca, Tommaso Argentini *

Politecnico di Milano, Department of Mechanical Engineering, via La Masa 1, 20156 Milano, Italy

ARTICLE INFO

Keywords:
Single-axis photovoltaic tracker
Solar plants
Aeroelastic response
Key parameters
Wind tunnel tests

ABSTRACT

Single-axis solar trackers enhance energy production and cost-effectiveness in large-scale solar installations compared to fixed panels. However, their structural design must address unique challenges, particularly regarding wind resistance, due to reduced mechanical properties for cost savings.

This article examines several key parameters of solar plants and evaluates their influence on tracker response, emphasizing wind-induced aeroelastic effects. These parameters include the layout arrangement of solar plants and the inter-row spacing. Tracker position has been evaluated in a 4-rows by 2-column corner region of rectangular tracker plant, with two ground cover ratios of 0.38 and 0.25. Moreover, the effects of the operational parameters of individual trackers have also been monitored, considering working pitch angles in the range between −60° and +60° and wind exposure angles of 0°, 15°, 30° and 45°. Structural properties were assumed to remain constant.

The research combines experimental wind tunnel tests with numerical dynamic simulations based on a finite element model, monitoring the internal stress state to assess performance.

Results show that large pitch angles (> 45°) exhibit stable aeroelastic behavior, while small pitch angles, between −30° and +30°, become unstable after reaching a certain velocity threshold. Among the monitored pitches, inclinations between 15° and 30° are the most critical in terms of internal response. The research confirms that trackers on the perimeter are the most stressed in the plants. The largest load cases occur with wind directions normal to the tracker axis. Finally, the analysis of the spacing between rows showed no significant effect on the response.

1. Introduction

In recent years, the global push towards sustainable energy solutions has fueled the rapid development of PhotoVoltaic (PV) plants as a viable means of harnessing solar energy and providing electricity on a large scale from clean and renewable resources. However, the effective implementation of PV plants comes with its own set of challenges and complexities. One of the primary concerns revolves around optimizing the design and configuration of PV plants to maximize energy output while ensuring cost-effectiveness. Single-axis solar trackers offer a promising solution to many of the challenges associated with the development and operation of PV plants. Unlike fixed-tilt PV modules, these systems track the sun's movement by dynamically orienting solar panels along an axis, addressing the issue related to solar irradiance variability.

The most common and viable type of single-axis tracker rotates around a North-South axis, tracking the sun from East to West [1]. These trackers typically consist of a longitudinal torsional tube supporting multiple solar panel modules, elevated above ground by vertical posts. Motor drives installed on these posts adjust the panels' inclination (also known as pitch or tilt angle). Although single-axis installations usually occupy less ground compared to fixed-tilt systems [2], their ability to maintain better alignment with the sun allows for greater power production. This results in more efficient land use by minimizing the land footprint and increasing energy yield per unit area [3].

From a structural perspective, PV systems (both fixed-tilt and tracking types) must be designed to withstand environmental loads, particularly extreme winds. PV systems are highly affected by turbulent wind fluctuations, which increase near ground level, according to typical turbulent profiles. Manufacturers aim to optimize return on investment by minimizing material use in these structures, resulting in lightweight assemblies that are more susceptible to turbulent wind forces acting on the large surfaces of the panels. Therefore, accurately evaluating the expected loads on these systems is crucial for proper structural design.

Wind action characterization involves isolating a static component, associated with the mean wind speed, from a dynamic component,

* Corresponding author.
E-mail address: tommaso.argentini@polimi.it (T. Argentini).

https://doi.org/10.1016/j.solener.2024.113232
Received 25 July 2024; Received in revised form 6 December 2024; Accepted 28 December 2024

List of recurring symbols

a_2^*, a_3^*	Flutter derivatives
B	Tracker chord
C	Tracker plant Column ($C = 1$ is a border column)
f	Structural frequency
$\mathbf{f}(t)$	Fluctuating zero-mean load acting on the system
H	Height above ground of the tracker's toque tube
i	Number of the structural mode of vibration
j	Identifier of a torque tube cross-section
L	Tracker length
L_j	Tributary length of cross section j
n	Number of modes considered
n_{sect}	Number of cross section considered along the torque tube axis
$\mathbf{q}(t)$	Principal coordinates describing structural response in modal reference system
$\mathbf{Q}(t)$	Lagrangian component of the applied loads
R	Tracker plant Row ($R = 1$ is a leading row)
U	Incoming wind velocity
U_N	Projection of the incoming wind velocity normal to the tracker's axis
U_R	Wind velocity experienced by a tracker in a generic row R
U^*	Reduced normal wind velocity $U_N/(Bf)$
$\mathbf{x}(t)$	Structural displacement due to buffeting and aeroelastic contribution
α	Exposure angle (i.e., wind direction)
β	Pitch angle (i.e., inclination of the tracker's panels)
ζ	Structural damping ratio
θ_j	Torque tube rotation about tracker's longitudinal axis
$\boldsymbol{\phi}_i$	ith mode shape
$[\Phi]$	Mode shape matrix

associated with time-varying fluctuations induced by turbulence, which can lead to resonant structural responses. The evaluation of the turbulent effects is numerically carried out using a buffeting response analysis, a well-established method in literature for applications such as aeronautical, bridge, and building design [4–9].

For PV structures, the buffeting forces are closely related to the panels' inclination angle. Additionally, certain inclination angles in PV tracking systems can induce significant aeroelastic effects due to the interaction between structural response and incoming wind flow, thereby influencing the dynamic response through aerodynamic stiffness and damping [10]. This necessitates corrections to the quasi-static theory by incorporating unsteady aerodynamic (or flutter) derivatives [11–13], which account for the coupling between wind flow and structural motion.

Most literature currently available concerning wind loads and structural design of PV systems, however, refers to fixed-tilt ground mounted installations. Early commercial studies [14,15] conducted feasibility analyses of PV plants under wind loads to assess cost reduction strategies. In these same studies, a potential complexity of the wind flow was also observed. In both researches, atmospheric boundary layer (ABL) wind tunnel tests were performed to characterize the wind loads; specifically [14] measured the wind actions (base moment and forces) directly using force balances; while [15] evaluated the loads on the panels' surface by measuring the actual pressure distributions. More recent studies [16,17], also carried out in with wind tunnels, focused on the characterization of other aspects concerning fixed-tilted PV arrays: the study of [16], while primarily focusing on the application of roof-mounted systems, provided useful information by performing experimental test also on a ground-mounted array configuration, and evaluated the problem for different exposure angles at a fixed inclination angle of 20°. With a similar setup, [17] focused on the effect of the lateral and longitudinal spacing, performing investigation on a model ground-mounted PV plants comprised of 12 rows of panels at a fixed inclination of 25°.

In [18] the research focused on the effects of vortex shedding in arrays of ground-mounted, fixed-tilt PV modules. It was observed that PV panels are characterized by structural frequencies above 1 Hz, which is the typical limit for flexible and slender structures above which it was usually assumed that a structure is not affected by dynamic wind effects [19]. On PV panels however, it was observed that vortex shedding caused by flow separation in the leading rows upwind, produce dynamic wind effects that greatly influence the response. Starting from the second row, relevant buffeting and self-excitation were observed, at frequencies well above the 1 Hz limit.

Other than experimental testings, Computational Fluid Dynamics (CFD) simulations were also used in literature [20–25] to investigate the interaction of solar panels with wind, focusing on different topics such as the evaluation of mean wind loads, the effects of inter-row spacing and the shielding effects provided by border PV panels to the internal ones.

Once the wind effects have been characterized for the specific system, the design procedure usually involves the evaluation of Equivalent Static Wind Loads (ESWL). Similar to other structural engineering applications, the ESWL [26–29] are usually adopted in current practice for this kind of constructions: with this approach, a relevant structural response associated to the dynamic wind can be reproduced by loading the structure with a set of equivalent static loads. Generally, the ESWL used in the dimensioning of a PV systems are defined as a distribution of forces and moments acting along the tracker axis.

In recent years, technological progress and reduction in manufacturing costs have enabled the development of tracking systems as a viable alternative to traditional fixed-mount systems. These trackers, due to the reduced degree of constraints provided by the motors, are more flexible in comparison and consequently are more susceptible to other problems related to dynamic wind effects. If aeroelastic effects are negligible, the dimensioning ESWLs for PV trackers are usually obtained by means of a simplified approach which involves the adoption of synthetic information provided by the implementation of so-called Dynamic Amplification Factors (DAFs) [16,30]. With this approach the dynamic effects can be estimated in a simplified way, as only the spectrum of the acting pressure (or moment) and the modal characteristics of the tracker are used. By integrating along the tracker surface the pressure time histories recorded with experimental wind tunnel tests, the acting forces and moments coefficients are defined [30]. Such coefficients are largely used in practice due to the fact that they are extremely easy to share with designers and implement for the computation of ESWL once scaled to design values. However, the simplifications introduced in the formulation bring shortcomings which, in practice, limit the scope of application of the results. Firstly, the DAF approach is a single-mode methodology and second, the experimental pressure measurements performed for the evaluation are typically carried out only on rigid scaled models. It follows that the experimental results should be applied only if the wind-induced deflections are small and the tracker is not susceptible to aeroelastic effects (and torsional instabilities). It has been proved that, especially for lower pitch angles ($\lesssim 30°$), at typical design mean wind speed (in the order of 25 m/s), these constructions reach instability conditions regardless of the geometry and mechanical properties [31]. The application of the results of the simplified DAF approach without considering the complete tracker behavior, and more specifically the effects of its interaction with the wind flow, can thus lead to a design on the unsafe-side.

In order to counteract this problem, a different design procedure, able to account the self-excited response of the tracker, is adopted.

Implementing an approach similar to what is performed on bridge analysis, [10] illustrate how it is possible to derive a complete formulation, accounting also for the self-excited contribution, of the dynamic problem by combining the results of rigid-model and sectional model wind tunnel tests.

Following this methodology, the objective of the research is to develop a parametric study of the problem in order to define the influence of the operational parameters in the design of a PV plants. To do so, starting from a set of experimental measures, the stress state acting in the torque tube, obtained by the adoption of the complete formulation, will be evaluated and compared for a varying set of tracker positions, pitch angles, exposure angles, wind velocity and inter-row spacing. Following this comparison, the complete formulation will be also benchmarked against a simpler time history analysis characterized by no self-excited forces, with the aim to highlight the actual effects of the aeroelastic contributions and the range of velocities for which a more thorough study of the problem is required.

The presented research is structured as follows:

- In Section 2 the main characteristics defining the plants layout and the tracker properties are defined.
- In Section 3 the governing equation of the problem is defined and its main terms are described.
- In Section 4, starting from the problem definition, the stability analysis is discussed and the developed approach to integrate and evaluate the structural response is presented.
- In Section 5 the presented procedure is adopted to evaluate the response for different sets of configurations, the main results obtained are then presented and commented.
- In Section 6, known aspects that may limit the scope of applicability of the method are presented.
- In Section 7 the content of the research are summarized and conclusions are drawn from the obtained results.

2. Photovoltaic plants with trackers

The focus of this study is on photovoltaic (PV) or solar plants with tracking systems. These types of plants can be examined from two main perspectives: the overall layout and organization of the whole plants, and the specific geometrical, mechanical, and operational features of the individual PV trackers.

2.1. Plants layout

A key parameter in the evaluation of the tracker's response in PV plants is the tracker position. With reference to a generic rectangular layout, the position of each tracker can be identified with a row-column pair (R, C), as sketched in Fig. 1(a). Another parameter concerning the plant layout is the spacing between adjacent tracker rows, which is often inferred from the *Ground Cover Ratio* parameter (GCR). In this article, the GCR is computed as the ratio between the tracker chord and the inter-row spacing.

Other critical aspects of the layout, relevant to wind-induced response, are the incoming mean wind speed U and its direction α. Indeed, to optimize energy production, PV plants are usually designed with a layout where the longitudinal axes of the trackers enable east-to-west rotation. In this study, the exposure angle α is computed as the angle between the wind direction and the direction normal to trackers' longitudinal axes.

2.2. Single-axis tracker

An individual PV tracker can be characterized by a series of parameters related to different design aspects [31]: for the purpose of the present article, two groups are defined. The first set comprises fixed parameters determined by design choices, including geometrical aspects (longitudinal length, chord length, height above ground), mechanical properties (choice of cross-sections, materials, and connection systems), and the installation scheme (number of columns and position of the central motor).

The second set of parameters involves operational properties related to the inclination (pitch) angle of the tracker as shown in Fig. 1(b). While the rotational capability enhances energy production, it also influences the tracker's response to wind actions, since its torsional stiffness is reduced. Key operational parameters include the *stow position* angle and the design critical wind speed. When wind speeds exceed the critical velocity threshold, the tracking system rotates to a *stow position*, a configuration designed to withstand larger wind loads.

In a solar plant, all trackers are typically grouped into a small number of tracker typologies characterized by the same properties (usually no more than four). This approach allows for a uniform evaluation of all trackers and facilitates optimization of the structural design based on the obtained results.

For a specific tracker typology, relevant information can be obtained from a *Finite Element* (FE) model of the system. These models enable immediate evaluation of the structural mass and stiffness matrices, key quantities for the numerical modeling of the structural response. Additionally, modal analysis can be performed to identify structural modal frequencies and modal shapes [32]. Fig. 2 shows the FE model of a standard PV tracker with a central motor, highlighting the characteristic first anti-symmetrical torsional mode [32,33].

Additional details about the FE modeling of the tracker used in this research are provided in Appendix B.

Table 1
Park and tracker parameters investigated.

Parameter	Symbol	Values
Row number	R	1, 2, 3, 4
Column number	C	1,2
Exposure angle	α	0°, 15°, 30°, 45°
Ground Cover Ratio (chord length/inter-row spacing)	GCR	0.38, 0.25
Mean wind speed at the first row tracker's torque tube height	U	from 10 m/s to 23 m/s (0.5 m/s steps)
along-wind turbulence intensity	I_u	16%
Number of columns	–	9
Driving system	–	central motor
Tracker length	L	45 m
Chord length	B	4 m
Torque tube height above ground	H	2 m
Structural damping ratio	ζ_{str}	2%
Pitch angle	β	0°, ±15°, ±30°, ±60°

2.3. Case study

In the present research, all key aspects related to the plant layout are considered in the analysis of the structural response. Concerning individual trackers, the structural characteristics are kept constant, assuming a single typology of tracker for the entire PV plant, to highlight the effect of the other design parameters. Only the variation of the pitch angle is included in the analyses, since it strongly affects the aerodynamics of the trackers. Table 1 summarizes the main parameters investigated in the study for both plant and trackers, along with the range of values considered.

3. Governing equations

3.1. Equation of motion

The structural response of a generic solar tracker subjected to a time variant wind-load forcing term can be described by means of the classic equation of motion (1).

$$[\mathrm{M_{str}}]\ddot{\mathbf{x}}_{\mathrm{tot}}(t) + [\mathrm{C_{str}}]\dot{\mathbf{x}}_{\mathrm{tot}}(t) + [\mathrm{K_{str}}]\mathbf{x}_{\mathrm{tot}}(t) = \mathbf{f}_{\mathrm{tot}}(t) \quad (1)$$

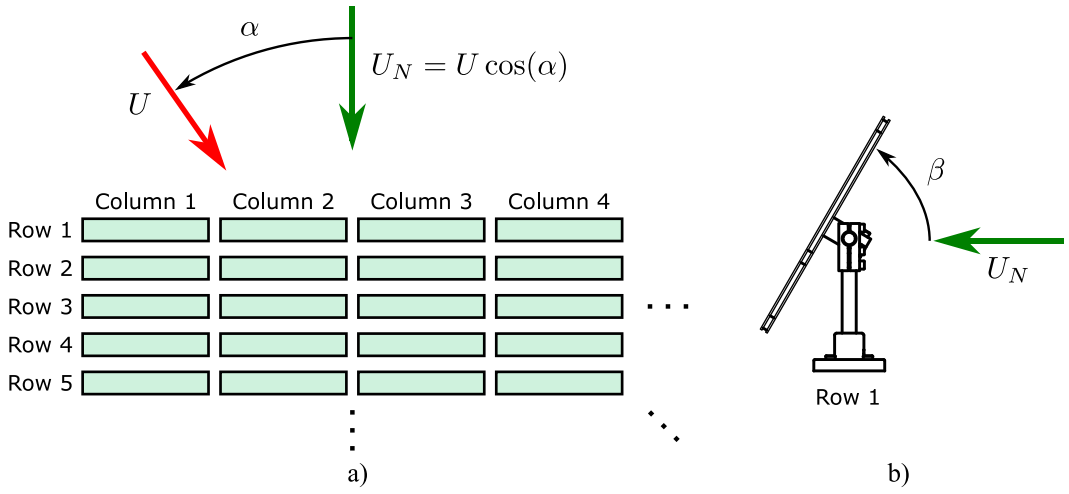

Fig. 1. Scheme of PV plant, (a) Top view,with definition of Row, Column, mean wind speed U, and wind exposure α; (b) Side view, with definition of pitch angle β.

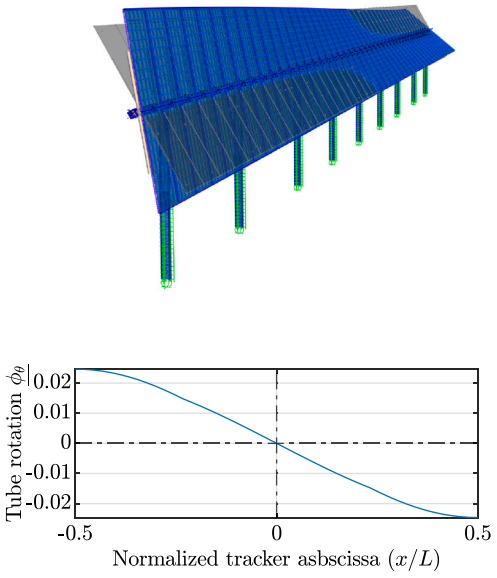

Fig. 2. FE model of a single-axis tracker showing the first anti-symmetrical torsional mode.

in which $\mathbf{x}_{\text{tot}}$ represent the total structural displacement vector, while $[\text{M}_{\text{str}}]$, $[\text{C}_{\text{str}}]$ and $[\text{K}_{\text{str}}]$ represent respectively the structural mass, damping and stiffness. While mass and stiffness matrices are easily obtained from the FE model, the evaluation of the structural damping $[\text{C}_{\text{str}}]$ is not as immediate, it is usually assumed referring to on-situ measurements on existing tracker installations of similar structural typology. Typical damping values adopted for the design of these structures have been observed to range between 2% and 5% [18,30,34,35].

It must be noted that the structural part on the left hand side remains unaltered for each tracker typology present in the plant. Thus, assuming only one structural typology, the same governing equation can be used for every tracker, changing only the wind-induced forcing term $\mathbf{f}_{\text{tot}}(t)$, that will be function of the different parameters reported in Table 1.

The equation of motion (1) can be conveniently solved by splitting the solution in a static component $\mathbf{x}_{\text{static}}$ plus a dynamic one $\mathbf{x}(t)$, which are respectively function of the static and dynamic components of $\mathbf{f}_{\text{tot}}(t)$, i.e. $\mathbf{f}_{\text{static}}$ and $\mathbf{f}(t)$.

The static problem $[\text{K}_{\text{str}}]\mathbf{x}_{\text{static}} = \mathbf{f}_{\text{static}}$ is straightforward, while the dynamic problem is usually solved using a modal approach, introducing the well-know modal superposition $\mathbf{x}(t) = [\Phi]\mathbf{q}(t)$. Indeed, introducing the modal shape matrix $[\Phi]$ and the vector of principal coordinates $\mathbf{q}(t)$ the dynamic problem can be written as:

$$[\tilde{\text{M}}_{\text{str}}]\ddot{\mathbf{q}}(t) + [\tilde{\text{C}}_{\text{str}}]\dot{\mathbf{q}}(t) + [\tilde{\text{K}}_{\text{str}}]\mathbf{q}(t) = [\Phi]^T\mathbf{f}(t) \tag{2}$$

where the $\sim$ symbol denotes that a matrix has been computed in modal reference system, and matrix $[\Phi]$ contains the modal shape vectors $[\boldsymbol{\phi}_1, \ldots, \boldsymbol{\phi}_n]$, being n the total number of modes considered in the analysis. Typically for these structure the first modes are associated to a torsional modal shapes with rotation about the longitudinal tracker axis, as shown in Fig. 2 where the first anti-symmetric torsional mode is reported as an example.

3.2. Force components evaluation

As previously introduced, the aerodynamic forces $\mathbf{f}_{tot}(t)$ are defined as the sum of a static term $\mathbf{f}_{\text{static}}$ and of two time-varying terms, namely the buffeting component $\mathbf{f}_{\text{buff}}(t)$, and the aeroelastic (self-excited) component $\mathbf{f}_{\text{aero}}(t)$.

Usually, the buffeting forces $\mathbf{f}_{\text{buff}}(t)$ (and their mean component $\mathbf{f}_{\text{static}}$) are measured experimentally by means of wind tunnel tests on rigid scale models of a solar plant

Fig. 3(a) shows an example of such model, which is equipped with pressure taps on the PV panels surfaces. Typical results of this experimental campaigns are time histories and maps of pressure distributions similar to the one reported in Fig. 4, where the effect of the pitch angle β, exposure angle α, and position (R, C) can be analyzed.

To simplify the problem formulation, the net pressure distribution resulting along the tracker's panel surface is integrated and summarized in a sectional normal force and a torsional moment pair, applied to/about the tracker center of rotation. The scheme in Fig. 5 depicts this simplification for a generic cross-section j. The ith Lagrangian component associated to the buffeting loads is thus computed as:

$$\boldsymbol{\phi}_i^T\mathbf{f}_{\text{buff}}(t) = \sum_j^{n_{\text{sect}}} \boldsymbol{\phi}_{i,j}\mathbf{f}_{\text{buff},j}(t) = Q_{i,\text{buff}} \tag{3}$$

where n_{sect} is the discrete number of cross sections in the numerical model used to apply the sectional loads, while $\boldsymbol{\phi}_{i,j}$ is the deformation of mode i observed at the jth cross section.

Further information on rigid model experimental tests is provided in Appendix A.1.

Aeroelastic forces ($\mathbf{f}_{\text{aero}}(t)$) are instead measured with experimental free-motion or forced-motion tests carried out on aeroelastic suspended sectional models with larger scale [35–37], as shown in Fig. 3(b). Due the geometry and the structural constraints of PV trackers, the

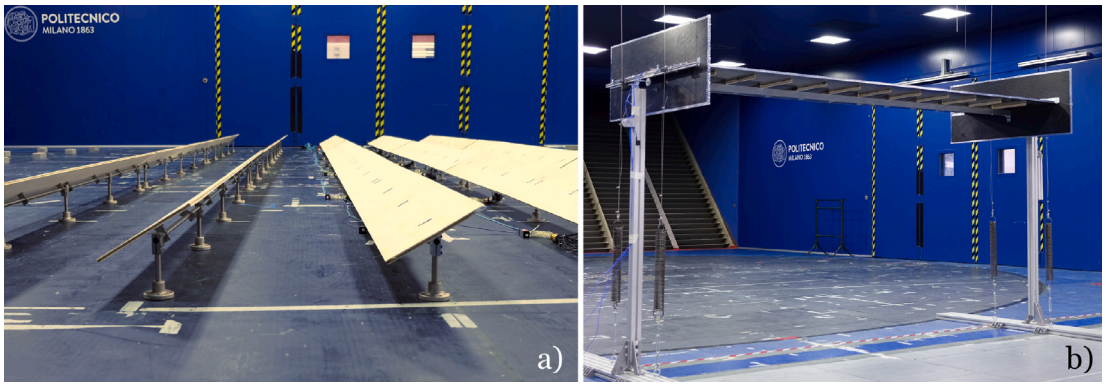

Fig. 3. Experimental Wind Tunnel models developed for the case study: (a) Rigid model (1:15 scale) of a PV plant portion for the pressure distribution evaluation (b) Free-motion experimental setup of the suspended sectional model (1:4 scale) for the identification of the flutter derivatives.

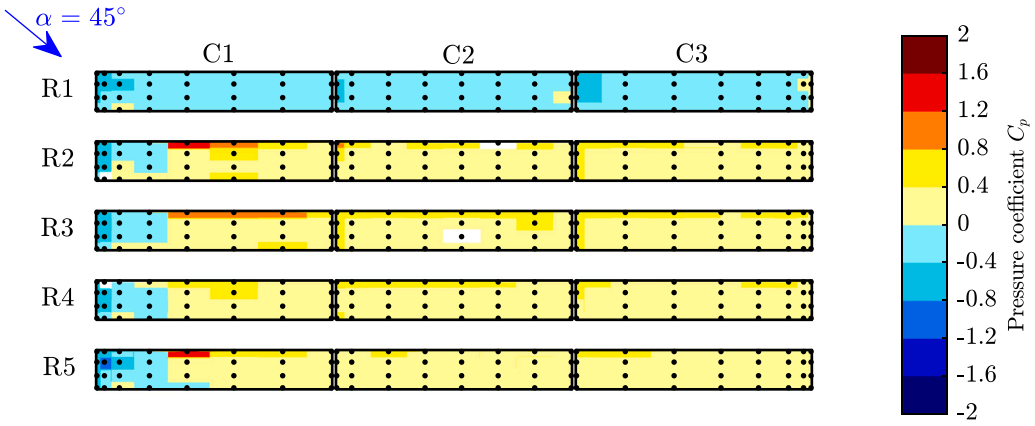

Fig. 4. Example of pressure distribution resulting from wind tunnel analysis on a rigid model, for $\beta = 60°$. Black dots indicate the position of the pressure measurements.

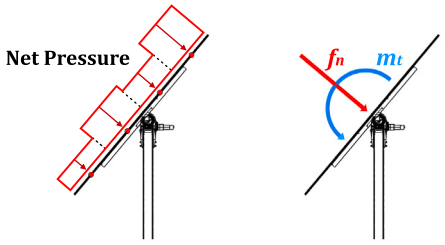

Fig. 5. Equivalent representation of the net pressure distribution acting on a panel into a normal force and torsional moment pair.

modes affected by self-excited contribution are generally limited to the torsional ones. Therefore the self-excited forces can be characterized solely by the aeroelastic moment due to the tracker rotation, while other forces and moments due to horizontal and vertical vibrations can be neglected [10].

Using the flutter derivative coefficients, usually adopted in bridge deck aeroelasticity [38,39], it is possible to define the aeroelastic moment acting on the jth tracker section $m_{t,\text{aero},j}$, by means of the flutter derivatives a_2^* and a_3^*, as:

$$m_{t,\text{aero},j} = \left(\frac{1}{2}\rho U_N^2 B^2 L_j\right) a_3^* \theta_j(t) - \left(\frac{1}{2}\rho U_N B^3 L_j\right) a_2^* \dot{\theta}_j(t) = -k_{\text{aero}}\,\theta_j(t) - c_{\text{aero}}\,\dot{\theta}_j(t) \quad (4)$$

where ρ is the air density, $U_N = U\cos(\alpha)$ is the component of the mean wind speed normal to the torque tube axis evaluated at the torque tube height (see Fig. 1), B the panel chord, L_j the section length, and θ_j is the torsional motion of the section. According to the notation reported in Eq. (4), it is possible to observe that at negative values of a_2^* corresponds to a negative aerodynamic damping for the system, while at positive values of a_3^* correspond a negative aerodynamic stiffness [40].

The a_2^* and a_3^* coefficients are function of the mean pitch angle of the section β_j and of the reduced velocity $U^* = U_N/(f\,B)$, being f the frequency of motion. These coefficients are defined experimentally as $a_{2,3}^* = a_{2,3}^*(\beta, U^*)$ for a discrete number of inclination β of the sectional model and incoming reduced wind velocity U^*. Fig. 6 shows, as an example, the results of the experimental test: a colormap describing $a_{2,3}^*$ coefficients is reported, where it can be observed that a nearest interpolation was used for intermediate values of the pitch angle.

Introducing the modal approach in Eq. (4), the ith Lagrangian component of the aeroelastic forces can be computed as:

$$\begin{aligned}\boldsymbol{\phi}_i^T \mathbf{f}_{\text{aero}}(t) &= \boldsymbol{\phi}_{i,\theta}^T \mathbf{m}_{t,\text{aero}}(t) = \sum_j^{n_{\text{sect}}} \phi_{i,\theta_j} m_{t,\text{aero},j}(t) \\ &= \sum_j^{n_{\text{sect}}} \phi_{i,\theta_j} \left[-k_{\text{aero},j}\,\theta_j(t) - c_{\text{aero},j}\,\dot{\theta}_j(t)\right] \\ &= -\left[\sum_j^{n_{\text{sect}}} \phi_{i,\theta_j} k_{\text{aero},j}\,[\boldsymbol{\Phi}_{\theta_j}]\right] \mathbf{q}(t) - \left[\sum_j^{n_{\text{sect}}} \phi_{i,\theta_j} c_{\text{aero},j}\,[\boldsymbol{\Phi}_{\theta_j}]\right] \dot{\mathbf{q}}(t) \\ &= -\mathbf{k}_{\text{aero},i}^T\,\mathbf{q}(t) - \mathbf{c}_{\text{aero},i}^T\,\dot{\mathbf{q}}(t)\end{aligned} \quad (5)$$

where ϕ_{i,θ_j} is the torsional deformation of the ith mode for the jth section, and $[\boldsymbol{\Phi}_{\theta_j}] = \left[\phi_{1,\theta_j}, \ldots, \phi_{n,\theta_j}\right]$. Considering all the n modes, the aeroelastic effects in modal coordinates can be synthetically written as:

$$\begin{aligned}[\boldsymbol{\Phi}]^T \mathbf{f}_{\text{aero}}(t) &= -\left[\mathbf{k}_{\text{aero},1}, \ldots, \mathbf{k}_{\text{aero},n}\right]^T \mathbf{q}(t) - \left[\mathbf{c}_{\text{aero},1}, \ldots, \mathbf{c}_{\text{aero},n}\right]^T \dot{\mathbf{q}}(t) \\ &= -[\tilde{\mathrm{K}}_{\text{aero}}]\mathbf{q}(t) - [\tilde{\mathrm{C}}_{\text{aero}}]\dot{\mathbf{q}}(t)\end{aligned} \quad (6)$$

where $[\tilde{\mathrm{K}}_{\text{aero}}]$ and $[\tilde{\mathrm{C}}_{\text{aero}}]$ are respectively the modal aeroelastic stiffness and damping matrices, which are in general full and not diagonal, and

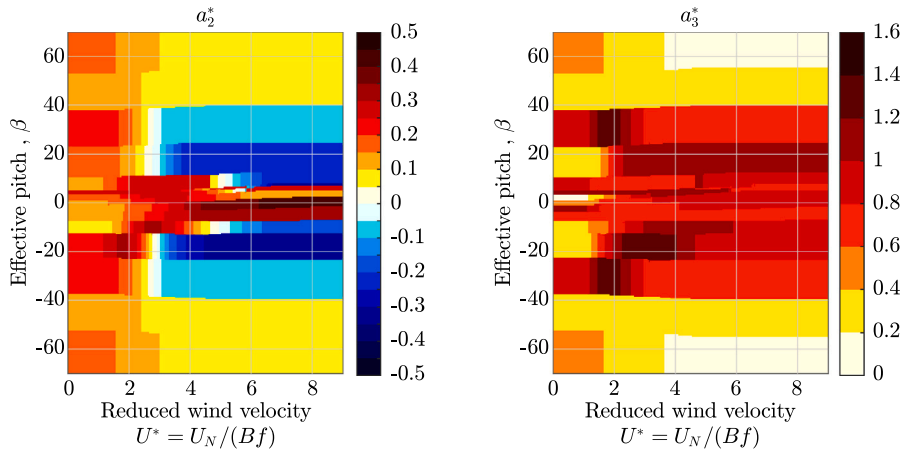

Fig. 6. Experimental flutter derivatives a_2^* and a_3^* for varying wind speed and pitch angle. $a_2^* < 0$ represents a negative aeroelastic contribution on the damping, while $a_3^* > 0$ represents a negative aeroelastic contribution on the stiffness.

which depend upon the reduced velocity and on the pitches of the different sections along the tracker.

Further information on the identification of flutter derivatives from free-vibration tests on suspended model is provided in Appendix A.2.

3.3. Aerolastically coupled modal equations of motion

Introducing Eqs. (3) and (6) into Eq. (2) the aeroelastically coupled modal equations of motion can be written as:

$$[\tilde{\mathrm{M}}_{\mathrm{str}}]\ddot{\mathbf{q}}(t) + \left([\tilde{\mathrm{C}}_{\mathrm{str}}] + [\tilde{\mathrm{C}}_{\mathrm{aero}}(\beta_j, U^*)]\right)\dot{\mathbf{q}}(t) + \left([\tilde{\mathrm{K}}_{\mathrm{str}}] + [\tilde{\mathrm{K}}_{\mathrm{aero}}(\beta_j, U^*)]\right)\mathbf{q}(t) = \mathbf{Q}_{\mathrm{buff}}(t) \tag{7}$$

where the total modal damping and stiffness matrices are the sum of the structural and aerodynamic ones, while the forcing terms are only related to the buffeting components.

4. Dynamic response

The aeroelastic equation of motion derived in Eq. (7) is an ordinary differential equation with constant coefficients. This equation can be used to conduct two primary types of analysis, which are discussed in detail in Sections 4.1 and 4.2. First, a stability analysis is performed to identify the stable and unstable ranges of the operational parameters concerning the aeroelastic response. Next, for the observed stability ranges, the structural response is computed using a time-domain approach.

4.1. Aeroelastic stability analysis

The stability of the tracker is studied solving, for every investigated value of wind speed U_N, the eigenvalue problem in the nearby of the mean configuration $\mathbf{x}_{static}$:

$$\left[[\tilde{\mathrm{M}}_{\mathrm{str}}]\lambda^2 + \left([\tilde{\mathrm{C}}_{\mathrm{str}}] + [\tilde{\mathrm{C}}_{\mathrm{aero}}(\beta_j, U^*)]\right)\lambda + \left([\tilde{\mathrm{K}}_{\mathrm{str}}] + [\tilde{\mathrm{K}}_{\mathrm{aero}}(\beta_j, U^*)]\right)\right]\underline{\Psi}_\lambda = 0 \tag{8}$$

where λ is the eigenvalue associated with the respective eigenvector $\underline{\Psi}_\lambda$. The solution of the eigenvalue–eigenvector problem requires an iterative non-linear procedure [41], since the system matrices depends upon the reduced velocity $U^* = U_N/(fB)$, which is intrinsically dependent on the eigenvalue λ, being the frequency of vibration $f = \mathbb{I}m(\lambda)/(2\pi)$ and the corresponding damping ratio value $\zeta = -\mathbb{R}e(\lambda)/|\lambda|$.

Considering a range of wind speeds U_N and a range of initial pitch angles β, the eigenvalues vary accordingly to the variation of flutter derivatives a_2^* and a_3^*, which depends upon U^* and the effective pitch angle of each tracker section that will be equal to β plus the mean rotation due to static aerodynamic forces. Such variation of eigenvalues provides relevant information regarding potential instabilities in the system due to wind–structure interaction. From a practical standpoint, characterizing the contributions of f and ζ is crucial for tracker design. Specifically, when either the total stiffness or total damping becomes negative, the structure becomes unstable: negative total stiffness corresponds to structural-static instabilities, while negative total damping corresponds to dynamic instabilities.

Therefore, performing the eigenvalue analysis for a range of initial pitch angles β and wind velocities normal to the tracker axis (U_N), it is possible to map the aeroelastic response for a combination of (U_N and β), producing a *stability map* as shown in Fig. 7.For combination of wind velocities and operational pitch angles in which both stiffness and damping are positive definite (green areas in the map), the system response is stable and the equation of motion can be integrated for further analyses to be performed. On the contrary, when the pair (U_N, β) produces a negative stiffness or damping the system solution is unstable and the structural response diverges (yellow and red areas).

To resist extreme wind effects, unstable cases are typically avoided in the design of the system by enforcing a specific operational pitch angle (*stow position*) when a critical wind velocity threshold is exceed. The larger ($|\beta| \geq 40°$) inclinations, are typically used for this purpose, since compared to smaller pitch angles, the responses is stable even at higher wind velocities.

Tracker systems shows also an overall stable response for $|\beta| = 0°$, it must be noted however that at higher velocities the pitch variation due to static loads (black lines in the color map) can change significantly the structural response, reaching an unstable behavior.

As an additional remark, it should be highlighted that for the computation of the reduced velocity U^*, the procedure refers to a mean wind speed, normal to the tracker axis, and computed at the torque tube height of the specific tracker row (R). Tracking systems in full-scale are arranged in arrays and due to the *shielding effect* provided by the leading rows upwind, the internal rows (R $\geq$ 2) can experience wind velocities lower than the first row ($U_R \leq U_N$). The flutter derivative maps of $a_{2,3}^*$ (Fig. 6) obtained by sectional model testing do not account for this effect since the test is performed on a single isolated tracker portion without obstacles upwind. By exploiting the rigid model simulations of the PV plant, it is possible to infer a reduction factor U_R/U_N of the inter-row wind speed. For this task, either a numerical procedure or experimental approach involving probes positioned between the model's rows [10], can be implemented to estimate the inter-row wind velocity field. Specifically for the case study developed in the present article, Fig. 8 shows the observed velocity reduction factor as a function of the plant row for a varying operational pitch angle: all internal rows

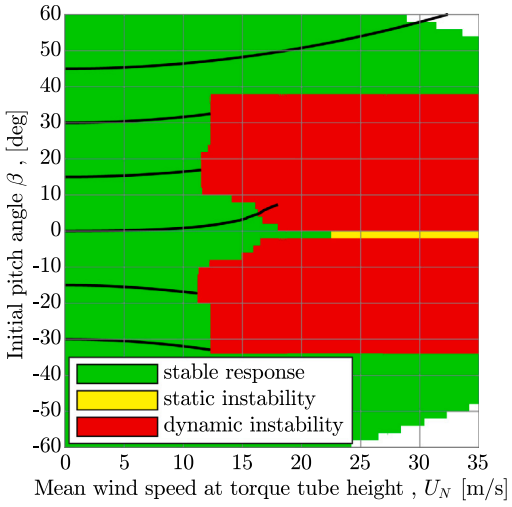

Fig. 7. Stability map depicting, the combinations of wind velocity and pitch angles that lead to either an dynamic instability (red) or a static instability (yellow) the PV tracker. Black curves represent the change in the effective pitch for a set of initial pitch angles. (For interpretation of the references to color in this figure legend, the reader is referred to the web version of this article.)

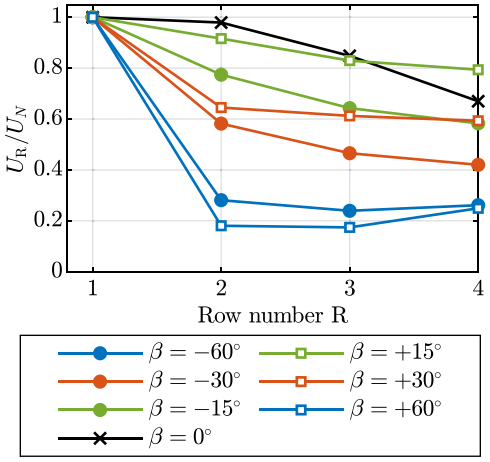

Fig. 8. Mean wind velocity reduction across the PV plant.

are subjected to a lower incoming mean wind speed, and this shielding effect is larger for larger pitch angles. It is therefore confirmed that the external rows at small pitch angles are the most critical elements for stability [31,35]. However, some design strategies aimed at economical effective solutions, might involve a different, less resistant, structural typology in the central part of the plant. In such cases also the internal tracker should be accounted for, due to its peculiar aeroelastic response.

4.2. Structural response evaluation

In stable operational conditions, the tracker behavior is investigated by numerically integrating the equations of motion in time domain. A standard 4th order Runge–Kutta numerical method is adopted, ensuring that the finite time step Δt used for the integration is small enough to accurately simulate the dynamic response.

In the simulations only stationary wind input and constant mechanical system properties were considered: the statistical indicators of the simulated wind and the structural properties of the trackers were assumed to do not evolve during the simulations.

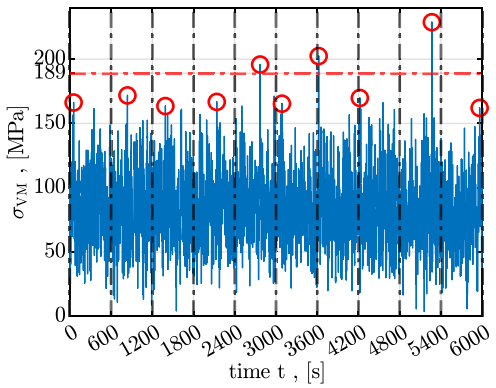

Fig. 9. Von Mises' stress time history: first row border tracker, central torque tube cross-section, $\alpha = 15°$, $\beta = 60°$, $U = 23$ m/s.

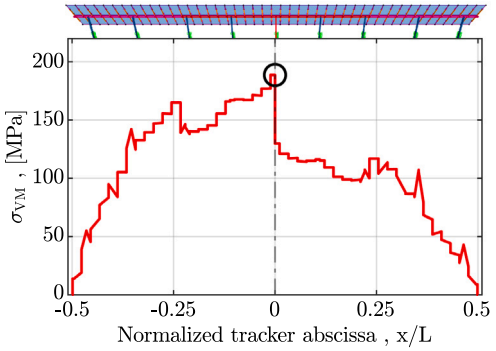

Fig. 10. Von Mises' stress evaluated along the tracker torque tube: first row border tracker R1 C1, $\alpha = 15°$, $\beta = 60°$, $U = 23$ m/s.

Provided that the pair of pitch angle and wind velocity lies in a stable region of the stability map, the solution of the equations of motion is a time history of the principal coordinates $\mathbf{q}(t)$, which can be easily used to infer the actual displacements and rotation in a physical reference system $\mathbf{x}_{tot}(t) = \mathbf{x}_{static} + [\Phi]\mathbf{q}(t)$.

From the knowledge of these structural displacements, internal actions and stresses time histories can be evaluated by exploiting the local structural stiffness and the geometrical properties of the structural elements (both easily obtained from the FE model implementation) and monitored to identify the most critical structural condition. Moreover, evaluating the internal stresses also opens the possibility for conducting a detailed fatigue analysis of structural components, ensuring their long-term reliability [42]. In the present article, the Von Mises' stress (σ_{VM}) computed along the tracker's torque tube was chosen as an indicator to evaluate the system internal response: the choice of this parameter is convenient since it allows to keep into account the effects of all internal actions.

Furthermore, to provide a more concise representation of the time histories, a single representative extreme value has been determined through statistical inference (e.g., [43–46]). For instance, in the current study the maximum and minimum values have been estimated with the Gumbel method for the evaluation of the extreme peak distribution, assuming a risk of exceedance of 22% [45]. Considering the σ_{VM} time history for the central cross section of a tracker torque tube, Fig. 9 shows the peak occurrences and the estimated extreme value from the underlying distribution. Here, the markers show the peak realizations in each of the time intervals, while the horizontal dashed line represents the statistical peak value.

By iterating the approach for each cross section along the tracker length, it is possible to derive an envelope representing the extreme

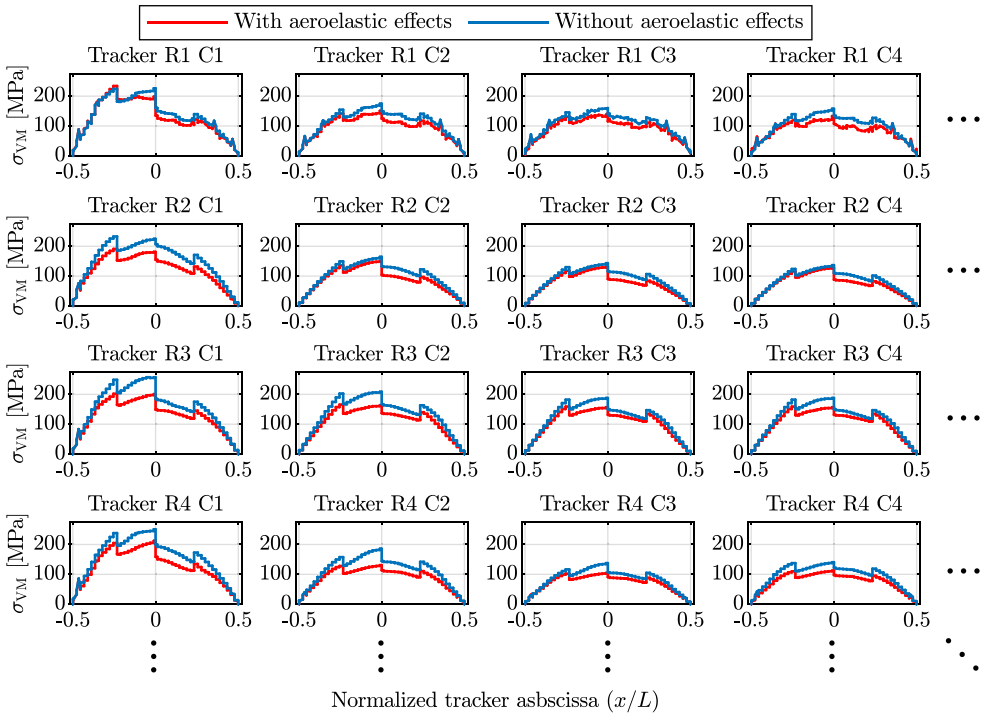

Fig. 11. Envelope for all exposure angles of Von Mises' stress acting in a portion of a generic PV plant, $\beta = 60°$, $U = 23$ m/s.

peak expectation of the Von Mises' stress for varying positions on the tracker's torque tube. Fig. 10 shows as an example the measured envelope of σ_{VM} for the tracker typology analyzed in the present research, for a specific configuration. In the observed trend, it is possible to notice a step in the central cross section ($x/L = 0$) characteristic of solar trackers equipped with a single central motor. The maximum value, observed in the center of the envelope diagram, is referenced in the following results comparisons, for each configuration considered in the study.

5. Assessment of PV plant and tracker response

Using the simulation framework presented so far, this section discusses the dynamic performance of the trackers in a photovoltaic plant. As outlined in Section 2.3, the focus is on the plant layout and operational parameters, while the structural and geometrical properties of the trackers are assumed constant across all simulations.

Additionally, the structural response of the trackers obtained by neglecting the self-excited contribution is analyzed against the response computed with the complete formulation of the equation of motion. This comparison highlights the importance of these terms in the modeling and assessment of the tracker performance.

In Section 5.1, the effect of the tracker position is discussed. In Section 5.2, the variation in response is evaluated in relation to different incoming wind speeds. Section 5.2.1 further develops this topic by comparing internal stress trends with the results of a simplified formulation that disregards the self-excited contribution of the system.

In Section 5.3, a portion of the PV plant is analyzed, focusing on the incidence of the exposure angle on the tracker's internal stresses. Finally, in Section 5.4, the effect of the spacing between rows is investigated.

As already introduced, Table 1 summarizes the values and the range of variation of the most significant parameters adopted.

5.1. Effects of tracker position

The results obtained for a single tracker in Fig. 10 can be extrapolated to a larger number of trackers within a PV plant. For example, Fig. 11 depicts the Von Mises' stress for the four leading rows and four border columns in a corner region of the PV plant. It should be noted that to account for different wind directions, the reported data have been enveloped for all the tested exposure angles, while the pitch angle is kept constant at 60°. This strategy is typically adopted in PV plant analysis to simplify the available information and account for the unpredictability of wind directions. The effect of the exposure angle will be analyzed in Section 5.3. However, while wind directed normal to the tracker axis ($\alpha = 0°$) is typically the worst scenario for aeroelastic stability, this does not necessarily hold true for the buffeting component.

Fig. 11 also facilitates the investigation of the effects of tracker position within the PV plant array. It can be observed that, in the selected case, the highest stress response occurs in either the first two leading rows or the border columns, while further inside the PV plant, the measured stresses gradually decrease. Although the results shown refer to a specific set of parameters, this trend has been observed to hold true for other pitch angles as well.

Regarding the effect of the aeroelastic component, it can be observed that this contribution significantly impacts the response. This additional effect can reduce the internal forces, as shown in Fig. 11, but this trend may vary, as discussed later in Section 5.2.1.

5.2. Influence of wind speed for different pitch angles

In Fig. 12 the trend of the peak Von Mises' stress is reported for increasing values of the mean wind speed, up to a value of 23 m/s, which is a typical value for the structural design of PV trackers. Four different pitch angles ($0°, 15°, 30°, 60°$) at varying tracker position in the border column (from $R1C1$ to $R4C1$) are reported, while other parameters have been fixed to $\zeta = 2\%$ and $GCR = 0.38$. The reported data, which consist of the envelope of all exposure angles, show that,

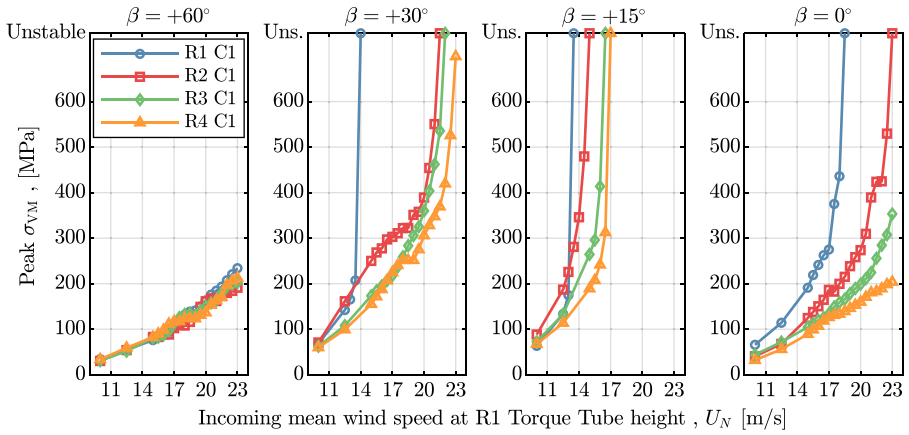

Fig. 12. σ_{VM} in the border column for increasing values of wind velocity, at different pitch angles; $GCR = 0.38$; envelope of all exposure angles.

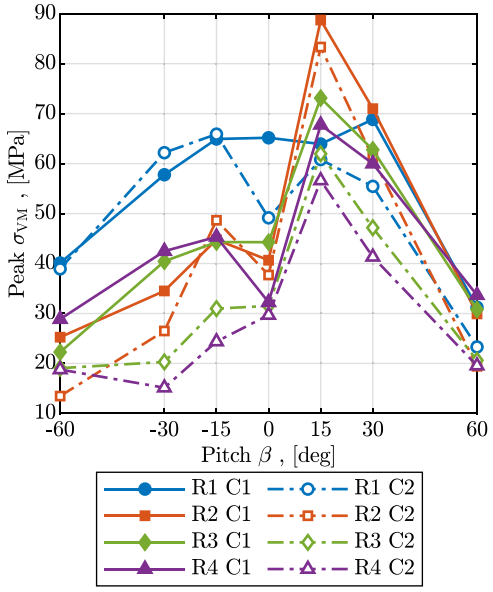

Fig. 13. Comparison of the peak σ_{VM} for different tracker position, varying pitch angle β; $GCR = 0.38$, $\zeta = 2\%$, $U = 10$ m/s, envelope of all exposure angles.

with respect to the mean wind speed, the tracker response can vary in a significant way based on the inclination of the PV modules.

The effects related to the wind velocity, other than the buffeting forcing term, also relate to the flutter derivatives adopted in the computation of the tracker self-excited response. In accordance with Fig. 7, at higher wind velocities, it is expected that the response may become unstable for certain pitch angles and diverge. Pitch angles of 30° and 15° highlight a rapid trend of the system to diverge with increasing mean wind velocities; compared to these two pitch angles, the case 0° shows a more stable response; still, at about 20 m/s, the tracker is again affected by instability. For such cases the dynamic instability is reached in the whole plant's border column when considering the maximum design wind speed.

On the contrary, at larger angles such as 60°, the response remain stable regardless of the incoming wind speed: the behavior is regular and can be also approximated by a linear trend. This observation is consistent with the stabilizing effect observed from the stability analysis (Section 4.1).

To highlight the dependence of the results on the pitch angle at a specific wind speed, the stress values of Fig. 12 can be plotted as reported Fig. 13. In this plot, the σ_{VM} are reported for varying pitch angle, considering a mean wind speed of 10 m/s, specifically chosen to have a stable response for all configurations. In addition to the previous dataset, the Figure reports also the response observed for negative pitch angles and the stresses evaluated in the second column of the PV plant (from $R1\,C2$ to $R4\,C2$). It is clear that for all tracker positions, the pitch angle of 15° is consistently the worst case among all the observed configurations. Moreover, for this specific inclination, it is possible to observe that the second row $R2$ displays larger responses compared to the other rows. This behavior is due to the combination of the small shielding effect provided by the leading row upwind ($R1$), and the additional buffeting forcing due to the turbulent wake of $R1$.

5.2.1. Contribution of the aeroelastic component

In current design practice, aeroelastic models are adopted to identify the stability range of the structure; then, under the assumption that the structural response remains in a stable region and the wind-induced deflections are small [30], coefficients resulting from rigid PV plant models are used in the evaluation of equivalent design loads. However, even assuming the structural behavior is stable, it does exist a range of wind velocities, lower than the critical wind speed, in which the structural response is meaningfully affected by the aeroelastic effects [10]. In this range, neglecting the self-excited contribution may have a relevant impact on the dynamic structural response and may lead to an underestimation or overestimation of the actual structural oscillations and thus internal response.

To highlight this effect, Fig. 14 reports, for three different tracker positions evaluated at three pitch angles, how the internal stress varies with the normal wind speed when the aeroelastic effects are included or neglected. Focusing specifically on the results obtained for the $R2C1$ tracker, it is possible to observe that for the largest angle $\beta = 60°$ the aeroelastic effects has a very minor effect regardless of the wind velocity. For $\beta = 30°$, a significant increment in the total damping is observed: for a wind velocity of 17 m/s, for example, the aeroelastic contribution leads to a reduction in the internal response by a factor of 2/3, compared to an evaluation carried out without self-excited contributions. Finally, for the angle $\beta = 30°$ the opposite is observed: the total structural damping is slightly decreasing with a trend approaching instability. At intermediate wind velocities, starting from 15 m/s, the structural response is still stable but an increment in the stress is observed; at 17 m/s, the response considering aeroelastic effects is of about 33% greater than without this contribution.

To generalize the observations, it is possible to note that similar considerations holds true also for the response trends reported in Fig. 14 for the two other tracker positions $R1\,C1$ and $R1\,C2$.

It is possible to conclude from the analysis of the reported data that, in some circumstances (e.g., large pitch angles and low velocities), methods which neglect the aeroelastic effects can be effective in

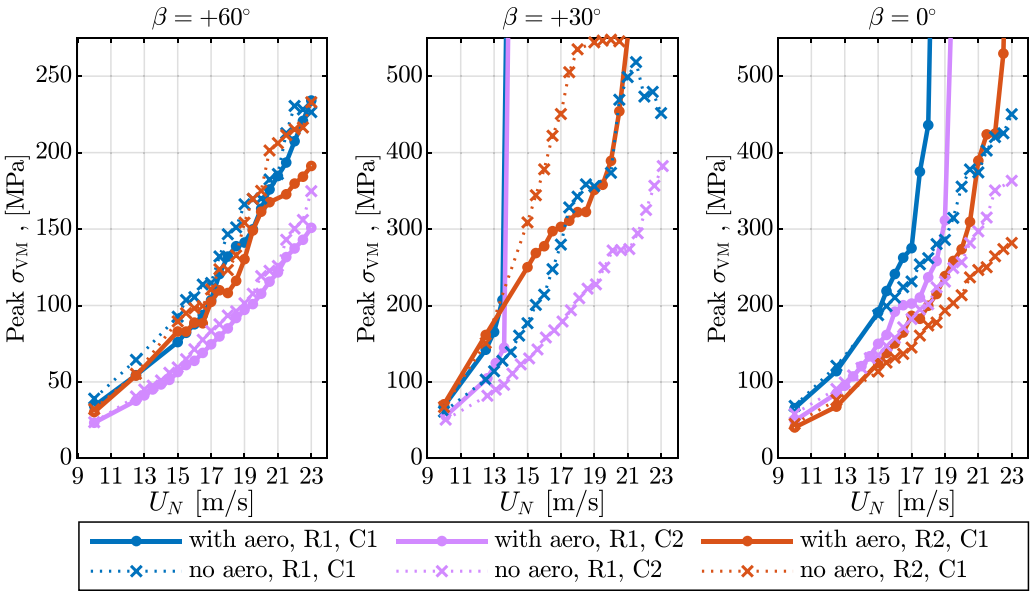

Fig. 14. Von Mises' stress for different values of wind velocity, considering and neglecting aeroelastic effects, at different pitch angle; $GCR = 0.38$, envelope of all exposure angles.

providing reasonable solution that deviates only slightly from the expected trend. However, it must be noted that given the observed trends for the lower pitch angles, a significant underestimation of the trackers' oscillations can be introduced leading to a wrong estimation of the stresses; for such cases, the "simplified methods" should implement adequate safety margins in order to account for the lack of the self-excited contribution.

5.3. Influence of the exposure angle

Analyzing individually the exposure angles α (as defined in previous Fig. 1), instead of adopting directly the envelope, could be of interest for determining at which wind direction the structural response is higher. Focusing on the border trackers ($C1$ and $C2$), Fig. 15 reports the trend of the Von Mises' stresses for different rows.

In the leading row ($R1$) it can be observed that for both the internal ($R1\,C2$) and corner ($R1\,C1$) trackers, the largest values are consistently recorded for the exposure values of $\alpha = 0°$ and $\alpha = 15°$. Moreover, concerning the corner tracker ($R1\,C1$), it can be also noted that, since the lateral side is exposed to wind, all the exposure angles have a relevant influence on the internal response.

The trend obtained is different on the second row $R2$. For most pitch angles the border tracker ($R2\,C1$) is characterized by values that are similar regardless of the exposure. However, positive pitch values in the range of [15°; 30°] present a particular case for which the Von Mises' stresses at the lower values of α (0°, 15°) are significantly larger than the other wind directions. A similar behavior is observed also in tracker ($R2\,C2$): the trend across all pitch angles remains the same, with the largest values recorder for $\alpha = 0°$ and gradually decreasing for higher values of exposure. Even though this tracker is shielded on both sides, the observed Von Mises' response for all pitch angles is not particularly different than the other perimeter elements.

The third row ($R3$) shows similar trends of the one observed on the first row. The largest values however do not appear to exceed the stress in the two leading rows, but remains non-negligible. Also the fourth row ($R4$) keeps the same trend observed before, but the values are smaller possibly due to the shielding effect provided by all the elements upwind.

Overall, it is possible to observe that the largest responses have been consistently measured at lower pitch angles across all monitored PV trackers, the largest responses have been observed on the 15° and 30° pitch angles. With the exception of the border tracker in the second row ($R2\,C1$) it is possible to observe that the first column is generally insensitive to the exposure angle, being this always exposed to incoming wind regardless of the direction. The second column, on the contrary, shows a more pronounced decreasing trend for increasing values of the α. Tracker $R2\,C1$ is particular since for the two pitch angles of 15° and 30° the response is remarkably high and the trend, other than being different with respect to other inclination angles, is associated to the largest response observed among all the monitored PV trackers; excluding these two pitch angles, however, previous observations still hold true.

5.4. Influence of the row spacing

With respect to the first three rows, a further analysis has been performed varying the spacing, also identified by the GCR parameter, defined in the scope of the present article as the ratio of the inter-row distance and the panel chord of the PV tracker. Fig. 16 reports the computed Von Mises' stresses for the selected trackers. It is possible to observe that the GCR has an influence, albeit generally limited, on the structural response: the results shows that for the case of $GCR = 0.25$ the σ_{VM} is marginally larger than the ones observed at $GCR = 0.38$. Contrary to other pitch angles, at $\beta = +15°$ and $\beta = +30°$ in the border tracker of the second row ($R2\,C1$) the trend seem to be reversed with the case $GCR = 0.38$ being slightly more severe than $GCR = 0.25$. The presented results seems to be consistent with the study of Warsido et al. [17], in which a trend in larger spacing being more critical than a shorter ones was observed when addressing the evaluation of the acting normal force and torsional in fixed-tilt solar plants.

6. Limitations of the study

Concerning the developed analysis, a series of challenging aspects may limit the scope of applicability of the observed results:

- Experimentation with model-scale sectional model is able to account only the aeroelastic effects observed by a first-row tracker with wind normal to its longitudinal axis. Extension of the analysis to internal trackers is performed by evaluating the reduction in mean wind velocity between each row due to the shielding effect provided by upwind trackers in the plant. This approach

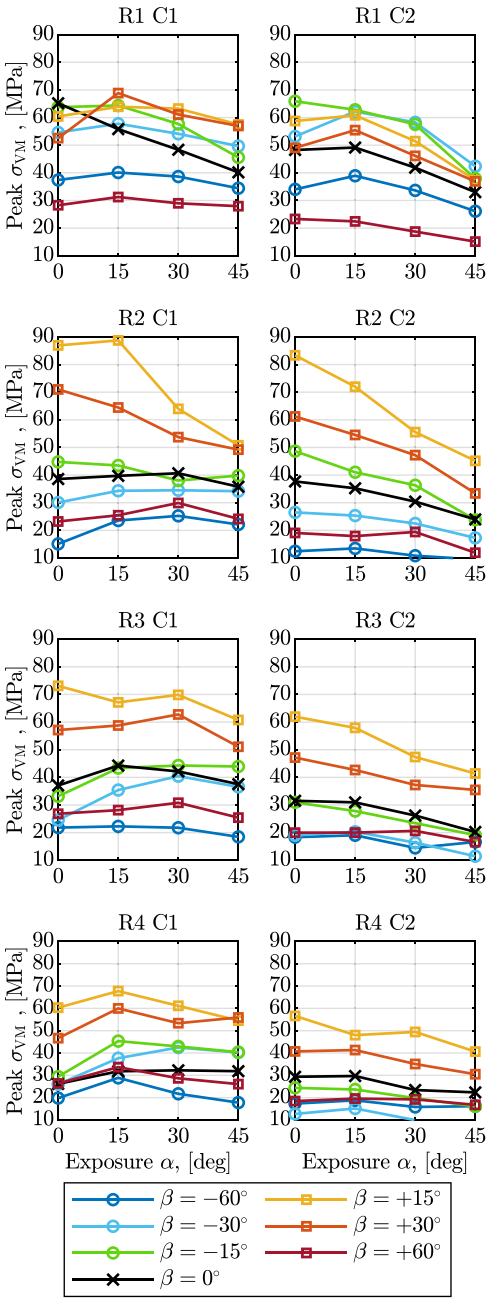

Fig. 15. Comparison of the maximum σ_{VM} for different exposure angle α and varying pitch angle β; $GCR = 0.38$, $U = 10$ m/s.

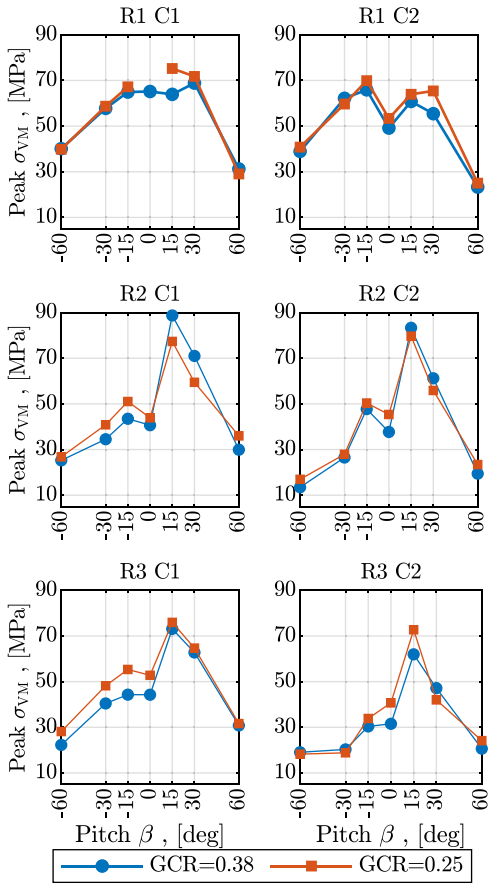

Fig. 16. Comparison of the maximum peak σ_{VM} for different GCR, varying pitch angle β and tracker position, $U = 10$ m/s; envelope of all exposure angles.

is typically conservative since the most severe effects is expected to occur on the first row. However, this approach is not able to account for the different wind flow characteristics in the inter-rows and, unexpected critical condition may arise from vortex shedding generated by leading trackers and cornering winds.

- The buffeting loads are computed assuming a rectangular layout for the PV plant, such simplification however is not directly transferable to cases in which the plant layout adapts to the available terrain, and it is not rectangular.
- Experimental tests and time domain simulations consider only stationary wind events characterized by a uniform wind velocity, turbulence intensity and integral length scale. Non-synoptic events, such as down-bursts, tornadoes and storms are not directly considered in the analysis. Specific assessments and adjustments in the method may be necessary if the power plant is installed in geographical regions characterized by such events.

7. Conclusions

The main objective of the presented research is the identification of how a selection of key operational parameters influence the structural response of PV trackers. To address this topic a parametric study has been carried out for varying quantities relevant for the design of PV plants; more specifically, the variables that were taken into account are the position inside a PV plant array, the wind velocity, the pitch angle, the exposure angle and the ground cover ratio. Starting from experimental data obtained through wind tunnel testing and a numerical model of a tracker, the dynamic equilibrium problem has been defined and numerically integrated. With respect to the specific problem definition, a complete system formulation, comprising both buffeting and self-excited contributions, has been implemented to account for the effects associated with wind–structure interaction.

With this approach, a stability analysis is performed initially to identify the wind velocity ranges in which the tracker behavior is stable at different pitch angles; for such cases, an assessment of the dynamic response then follows. To provide a concise summary of the results, the extreme peak estimate of the Von Mises' stress, acting along the torque tube axis, has been taken as an indicator representing the structural response.

With the aforementioned methodology, the tracker's behavior was computed and compared for the different sets of parameters. The main results are here summarized:

- Different tracker positions, comprising the first four columns and four rows starting from the corner region of a generic rectangular layout of a PV plant, were considered in the analysis. The study shows that the response distribution among the trackers can be attributed to different geometrical zones. The first row $R1$ and second row $R2$, for specific positive pitch angles, exhibit the largest observed stresses. From the third row $R3$ onward, no case provides a Von Mises' stress significantly larger than the two leading rows; this is due to the shielding effect provided by the perimeter elements, which generally lowers the wind velocity and consequently the resulting loads. The border region ($C1$), even when not associated with the most severe conditions, presents significant stress values, much larger than those measured inside the plant. For this reason, this zone should be specifically accounted for in the design process.
- Regarding the evaluation of the wind speed effects, a series of simulations were performed for a set of incoming mean wind speeds, evaluated in correspondence of the tracker's torque tube height, ranging from 10 m/s to 23 m/s, for pitch angles of 0°, +15°, +30° and +60°. It has been observed that large pitch angles are generally stable, and in this condition the Von Mises' stress increases with an almost linear trend with respect to the incoming wind speed. At the lower inclinations, problems may arise when a critical wind velocity is exceeded and the response is expected to become unstable and diverge.
- Extending the evaluation to different pitch angles, a comparison for seven inclinations (0°, ±15°, ±30° and ±60°) has been performed considering an incoming mean wind speed of 10 m/s, velocity specifically chosen to represent all available configurations in a stable range. In the evaluation the two border tracker for the first four leading rows have been considered. The results highlighted a strong influence of the structural response for varying inclinations. Pitch angle +15° appears to be the most critical configuration, with stresses values consistently high across all the trackers, while the largest pitch angles (±60°) provide low stress values. In addition it has been observed that positive inclinations (nose-up configuration) show consistent stress values across all monitored trackers compared to negative pitch angles.
- The results of a simplified formulation of the governing equation, which neglects the self-excited response, have been compared to the complete formulation of the problem. The purpose of this step is to assess the actual effects of the self-excited contribution and to compare with a simpler approach that should be closer to the methodologies currently used for the ESWL evaluation on PV structures. For cases in which the system is characterized by a stable behavior, such as large pitch angles (60°) or for lower wind velocities, the simplification provides a safe estimation of the monitored parameter; it must be noted that in this scenario overestimation of the response can occur and thus over-sizing of the structure, undermining possible economical savings in the production of these systems. For such cases, it must be noted that preceding the critical velocity, the response is still stable but a noticeable increment in the response is observed. It follows that neglecting the aeroelastic contribution leads to a significant underestimation of the stress state in such cases: special considerations must be given during dimensioning by considering adequate safety margins.
- Evaluating the response for four different exposure angles, ranging from 0° to 45° with 15° increments, the results show that the wind direction has a significant effect on the structural response of internal trackers. It is possible to generalize the observation by noting that the largest Von Mises' stresses were recorded for exposures of either $\alpha = 0°$ or $\alpha = 15°$, while larger exposures are generally associated with a lower influence on the structural response. With the exception of the second row, which appears to be the most critical position overall, the dependency on exposure is less pronounced for trackers in the border column $C1$. This is possibly due to the fact that the system is always exposed to incoming wind, resulting in a relatively constant peak response trend.
- A comparison of the spacing between adjacent rows has been performed by considering two GCR values, 0.25 and 0.38. Between the two sets of simulations, the larger spacing ($GCR = 0.25$) was observed to be slightly more unfavorable, but still with very limited difference, compared to the narrower spacing ($GCR = 0.38$).

The study focused on analyzing a range of operational parameters in the evaluation of the internal response. Additionally, if experimental tests were available and compatible with a full-scale problem, the proposed method could be easily extended to different chord lengths, tracker heights, and inter-row spacing. Furthermore, it is also possible to account for other sets of properties, such as structural stiffness due to the choice of cross-sections, total mass, and motor position. The ability to adapt the formulation to a multitude of parameters allows for the development of a useful benchmark tool to compare the performance of trackers, not only for operational working configurations but also for different design strategies.

Further research could delve into the effects of cornering winds and wind–structure interactions in multi-row configurations. This can be achieved through wind tunnel testing on aeroelastic model-scale tracker plants, enabling a more precise simulation of dynamic responses. In parallel, long-term, full-scale monitoring at an actual installation site could not only provide comparable insights but also yield valuable data for identifying key structural properties, such as the actual structural damping and natural frequencies of installed systems. Finally, computational fluid dynamics (CFD) analyses, informed by validated case studies, could offer deeper insights into flow characteristics, particularly for evaluating inter-row wind flow dynamics.

CRediT authorship contribution statement

Giorgio Frontini: Writing – original draft, Visualization, Software, Methodology, Investigation, Formal analysis, Conceptualization. **Filippo Calamelli:** Writing – review & editing, Visualization, Formal analysis. **Sara Muggiasca:** Writing – review & editing, Supervision, Resources, Investigation, Conceptualization. **Tommaso Argentini:** Writing – review & editing, Visualization, Supervision, Methodology, Investigation, Conceptualization.

Declaration of competing interest

The authors declare that they have no known competing financial interests or personal relationships that could have appeared to influence the work reported in this paper.

Appendix A. Experimental wind tunnel tests

The structural response of solar trackers and solar farms to wind loads is typically evaluated in a wind tunnel. These experiments also enable cost-effective assessments of various design configurations before field deployment.

A crucial aspect of such testing is the accurate characterization of the wind flow within the test section. Additionally, the scaling laws used in the tests must ensure that the results accurately represent full-scale conditions.

A.1. Rigid model of the PV model

In these experiments, a representative section of the solar farm, specifically the corner region, which is expected to experience the

highest wind loads, is reproduced at model scale and equipped with pressure taps on the surface. The key results of this experiment are the wind loads acting on the solar tracker, comprising the forces due to the mean incoming wind as well as the fluctuations induced by turbulence (buffeting), which depends upon the terrain characteristics in the nearby of the plant site. The scaled model is tested under diverse wind directions and pitch angles to evaluate the worst loading conditions on the system's surfaces. Structural properties (i.e., chord length and height above ground) and spacing in the plant layout are typically assumed fixed for an entire cycle of experimental test.

With rigid modeling, the test object is expected to not deform during the actual experimentation. This task is accomplished by assembling the scale model using rigid materials, such as carbon-fiber, wood and aluminum; such models are used to measure how the specific geometry of the test object influence the surface pressure due to the incoming wind flow. On rigid models, the main instruments typically used for the experimental assessment are pressure scanners: with each scanner many acquisition points distributed on the model surfaces, can be acquired simultaneously, enabling for extensive portions of the model to be measured.

In the analyzed case study, the plant were reproduced in 1:15 scale with a rigid model equipped with 512 pressure acquisition points (pressure taps). All the acquisition points were, in bundle of 32, connected by means of a PVC tubing to sixteen ESP 32HD miniaturized pressure scanners. Closing the acquisition chain, two analog-to-digital acquisition systems have been used to record the pressure time histories with a sample rate of 500 Hz.

To provide data which can be scalable to different geometries for design purposes, the physical measurements are provided in terms of non-dimensional coefficient as in Eq. (A.1).

$$C_{p,jk}(t) = \frac{p_{jk}(t) - p_0}{\frac{1}{2}\rho U^2} \tag{A.1}$$

where p_{jk} is the absolute pressure measured at cross-section j and position k; p_0 is the static pressure in the wind tunnel test section and U is the mean component of the incoming wind speed (i.e., before interacting with the model) at a reference height. Considering the difference between the pressure observed on the two sides of the model panels, for each acquisition point, the net pressure p^{net} can be inferred. The net pressure distribution along the tracker can be easily transformed into a distribution of normal force and torsional moment, as sketched in Fig. 5.

A.2. Aeroelastic suspended sectional model

The two coefficients a_2^* and a_3^* are typically evaluated through wind tunnel sectional models with either free-motion or forced motion test [36]. In this study, experimental measurements were performed adopting the free-motion test methodology on a sectional tracker model and analyzing the oscillation frequency and the total damping post-processing the system response, obtained for a range of velocities and initial inclination angles [47–49].

Due to the nature of solar trackers, where the inclination angle of the panel surface can vary significantly during operation, it is essential to properly account for the variation in the mean pitch angle, as it has a substantial impact on the self-excited response.

In Fig. 3(b) the experimental setup developed in Politecnico di Milano Wind Tunnel is shown: a clamping system is used to fix the model tracker section in an initial position; four springs per side, connected to the end plates of the model, allows the PV panel to oscillate around the initial configuration. The rotation about the longitudinal axis was reproduced with a structural damping ratio of $\zeta_\theta = 2\%$.

Using Eq. (4) as a reference and applying it to a sectional model, the formula can be inverted to express the two coefficients as follows:

$$\begin{cases} a_2^*(\beta;U^*) = \dfrac{4J[\omega_\theta(\beta;U^*)\cdot\zeta_\theta(\beta;U^*) - \omega_\theta(\beta;0)\cdot\zeta_\theta(\beta;0)]}{\rho U B^3} \\ a_3^*(\beta;U^*) = \dfrac{2J[\omega_\theta^2(\beta;0) - \omega_\theta^2(\beta;U^*)]}{\rho U^2 B^2} \end{cases} \tag{A.2}$$

Where J is the mass moment of inertia per unit length evaluated about the axis of rotation of the panel surface. $\omega_\theta(\beta;U^*) = 2\pi f_\theta(\beta;U^*)$ represents the angular frequency of the system, for a given initial pitch angle β and reduced velocity $U^* = U/(fB)$. Likewise, $\zeta_\theta(\beta;U^*)$ is the rotational damping for the same combination of pitch angle and reduced velocity. From the adopted definition of the flutter derivatives [40] positive values of a_2^* represent an increment to the initial structural damping due to the interaction between wind flow and structural response; concerning a_3^* positive values represent a decrease of the initial structural stiffness due to the same coupling. As an example, Fig. A.17 shows the trend of the flutter derivatives as a function of the wind speed, for initial pitch angle $\beta = -30°$. The complete set of coefficients is reported in Fig. 6 as a color map.

A.3. Stability considerations

Considering only the torsional model for simplicity, the eigenvalue problem of Eq. (8) can be solved as a function of the incoming wind speed U_N, to find the evolution of the frequency (stiffness) and damping. As an example, a typical trend is shown in Fig. A.18, where, for the pitch angle $\beta = -30°$, the trend of total torsional stiffness (relative to structural) and damping ratio are reported as a function of the wind speed. These trends indicate whether the mechanical system becomes unstable and the type of instability that occurs. A negative total stiffness corresponds to static instabilities, while a negative total damping corresponds to dynamic instabilities. In this example, a dynamic instability occurs at 12.2 m/s, as the total damping becomes negative for higher wind speeds.

Performing the analysis for a range of pitch angles, β, and wind velocities, U_N, produces a stability map, such as the one shown in Fig. 7.

Appendix B. FE model description

The definition of the structural stiffness [K_{str}] and mass matrices [M_{str}] is typically inferred directly from an finite element model. In current practice, this easily accomplished since the numerical model is a result of prior design stages.

The evaluation of the structural damping [C_{str}], however, is not as immediate, but previous measurements on existing tracker of similar structural typology can be used, if specific in-situ test campaigns are not used.

Given the tracker's geometrical regularity, the tracker FE model can be systematically generated with a computational routine for a given set of structural and geometrical parameters; this approach allows for a faster model generation when changing a single property of the entire tracker, such as chord dimensions and spacings. The main features taken into account into the FE model generation procedure are as follows:

- Tracker generalities: Tracker pitch angle and number of PV panels.
- Posts: Cross sections, number, location, height, terrain stiffness.
- Torque tube: Cross sections, length of the different portions (if any), changes in thickness.
- Supporting beams: Cross sections, length, number of connection point with torque tube and PV panel frames.
- PV panels: Dimensions, Glass thickness, frame height, spacing.

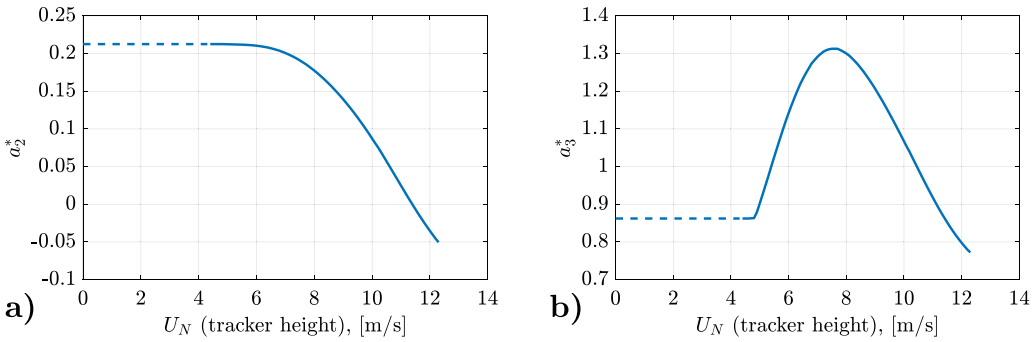

Fig. A.17. Flutter derivatives a_2^* (a) and a_3^* (b) for pitch $\beta = -30°$, for increasing wind velocity (in this case, values for wind speed < 4 m/s are extrapolated constant).

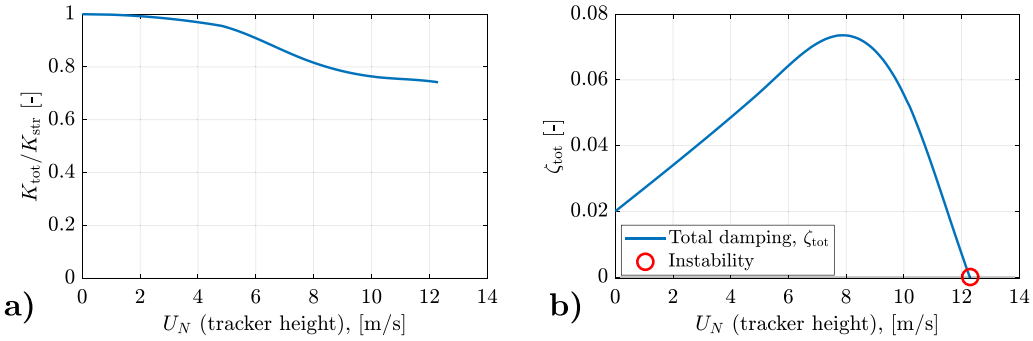

Fig. A.18. Stiffness ratio (a) and total damping ζ_{tot} for pitch $\beta = -30°$, for increasing wind velocity.

The main geometrical features of the analyzed case study are reported in Table B.2.

In the definition of the tracker, particular attention was focused on the accurate reproduction of the structural detailing to provide reliable results with respect to the case specific reference. More specifically the considerations that were made involved the following aspects:

- *Geometrical consistency*: The different structural elements composing the tracker are inserted in accordance with specification and avoiding possible overlapping. Doing so ensures that the correct eccentricity of the elements with respect to the tracker torque tube is kept.
- *PV Panel representation*: Each photovoltaic panel is modeled as a single shell element supported directly by its frame. In accordance with specification, each panel is an individual structural entity: spacing between adjacent PV modules has been kept.
- *Beam-Panel connection points*: By specification, the PV panels are connected to supporting beams by means of riveted or bolted connections in specified point. This connection in the FE model has been enforced introducing rigid links between supporting beams and panel frames at the appropriate locations. The definition of these connection points restores the structural continuity of the tracker.
- *Simple support of the columns*: With the exception of the motorized column, the tracker's posts behave as simple supports that allows for the tracker to freely rotate about the longitudinal axis. To correctly represent the structural response, the transmission of the torsion from the shaft to the supporting posts was prevented introducing frame releases in the column joints.
- *Soil modeling*: The soil–structure interaction has been accounted for in the FE model with the introduction of linear springs of stiffness increasing with the depth connected to the infixed portion of the vertical columns. In the developed analysis however, this contribution was neglected assuming that the tracker is fixed at ground level.

Table B.2
Geometrical features of the FE model.

Parameter	Values
Tracker length	45 m
Torque tube height (above ground)	2 m
Number of columns	9
Driving system	central motor
Panel configuration	2-in-portrait (2P)
Chord length	4 m
Torque tube dimensions (tracker's center)	square $150 \times 150 \times 4$ mm
Torque tube dimensions (extending for 12 m from extremities)	square $150 \times 150 \times 3$ mm
Supporting beam height	100 mm
PV panel dimensions	0.9 m × 1.98 m
PV frame thickness	40 mm
Structural material	Steel S355
Terrain stiffness	rigid

Table B.3
First structural frequency from FE model.

Mode	Type	Frequency [Hz]
1	1st torsional	1.2
2	2nd torsional	1.2
3	3rd torsional	3.2
4	4th torsional	3.3
5	1st flexural	4.4
6	5th torsional	5.1

The assembled FE model allows the designers to perform modal analyses to identify also the modal shapes ϕ_i and the associated structural frequencies f_i. As an example, the first structural frequencies with rigid terrain are reported in Table B.3, while Fig. B.19 reports for the first three modes the corresponding modal shapes.

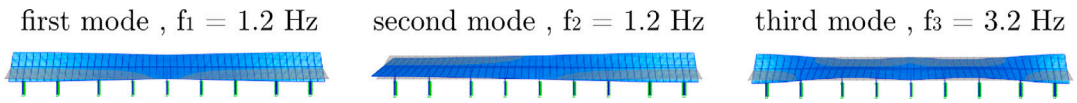

Fig. B.19. First three modes of the tracker, FE model of Fig. 2.

References

[1] A. Barbón, P.F. Ayuso, L. Bayón, C. Silva, A comparative study between racking systems for photovoltaic power systems, Renew. Energy 180 (2021) 424–437, http://dx.doi.org/10.1016/j.renene.2021.08.065.

[2] A. Barbón, V. Carreira-Fontao, L. Bayón, C. Silva, Optimal design and cost analysis of single-axis tracking photovoltaic power plants, Renew. Energy 211 (2023) 626–646, http://dx.doi.org/10.1016/j.renene.2023.04.110.

[3] P.H.A. Veríssimo, R.A. Campos, M.V. Guarnieri, J.P.A. Veríssimo, L.R. do Nascimento, R. Rüther, Area and LCOE considerations in utility-scale, single-axis tracking pv power plant topology optimization, Sol. Energy 211 (2020) 433–445, http://dx.doi.org/10.1016/j.solener.2020.09.070.

[4] A. Davenport, The response of slender, line-like structures to a gusty wind, Proc. Inst. Civ. Eng. 23 (1962) 389–408, http://dx.doi.org/10.1680/iicep.1962.10876.

[5] H. Irwin, K. Cooper, R. Girard, Correction of distortion effects caused by tubing systems in measurements of fluctuating pressures, J. Wind Eng. Ind. Aerodyn. 5 (1979) 93–107, http://dx.doi.org/10.1016/0167-6105(79)90026-6.

[6] F. Calamelli, R. Rossi, T. Argentini, D. Rocchi, G. Diana, A nonlinear approach for the simulation of the buffeting response of long span bridges under non-synoptic storm winds, J. Wind Eng. Ind. Aerodyn. 247 (2024) 105681, http://dx.doi.org/10.1016/j.jweia.2024.105681.

[7] G. Diana, D. Rocchi, T. Argentini, Buffeting response of long span bridges: numerical-experimental validation of fluid-structure interaction models, in: IABSE Conference - Structural Engineering: Providing Solutions To Global Challenges, International Association for Bridge and Structural Engineering (IABSE), Geneva, Switzerland, 2015, pp. 2141–2147, http://dx.doi.org/10.2749/222137815818359618.

[8] G. Diana, D. Rocchi, T. Argentini, Buffeting response of the izmit bay bridge: Numerical and experimental results, in: Proceedings of the Istanbul Bridge Conference, 2014.

[9] T. Argentini, M. Belloli, F. Fossati, D. Rocchi, M. Villani, Experimental and numerical analysis of the dynamic response of cable-stayed bridge: vortex induced vibrations and buffeting effects, in: 13th International Conference on Wind Engineering, IAWE, Amsterdam, The Netherlands, 2011.

[10] Z. Taylor, M. Browne, Hybrid pressure integration and buffeting analysis for multi-row wind loading in an array of single-axis trackers, J. Wind Eng. Ind. Aerodyn. 197 (2020) http://dx.doi.org/10.1016/j.jweia.2019.104056.

[11] R.H. Scanlan, A. Sabzevari, Experimental aerodynamic coefficients in the analytical study of suspension bridge flutter, J. Mech. Eng. Sci. 11 (1969) 234–242, http://dx.doi.org/10.1243/JMES_JOUR_1969_011_031_02.

[12] R.H. Scanlan, J.J. Tomko, Airfoil and bridge deck flutter derivatives, J. Eng. Mech. Div. 97 (1971) 1717–1737, http://dx.doi.org/10.1061/JMCEA3.0001526.

[13] G. Diana, S. Stoyanoff, A. Allsop, L. Amerio, M.S. Andersen, T. Argentini, F. Calamelli, M.C. Montoya, V.d. de Goyet, S. Hernández, J.Á. Jurado, I. Kavrakov, G. Larose, A. Larsen, G. Morgenthal, D. Rocchi, M.N. Svendsen, T. Wu, IABSE task group 3.1 benchmark results. Numerical full bridge stability and buffeting simulations, Struct. Eng. Int. 33 (4) (2023) 623–634, http://dx.doi.org/10.1080/10168664.2022.2104188.

[14] I. Bechtel National, Wind Design of Flat Panel Photovoltaic Array Structures. Final Report, Technical Report, Bechtel National, Inc., 1980, URL: https://www.osti.gov/biblio/5146308.

[15] R. Miller, D. Zimmerman, Wind loads on flat plate photovoltaic array fields. Phase III, final report, 1981, http://dx.doi.org/10.2172/6782774.

[16] G. Kopp, S. Farquhar, M. Morrison, Aerodynamic mechanisms for wind loads on tilted, roof-mounted, solar arrays, J. Wind Eng. Ind. Aerodyn. 111 (2012) 40–52, http://dx.doi.org/10.1016/j.jweia.2012.08.004.

[17] W.P. Warsido, G.T. Bitsuamlak, J. Barata, A.G. Chowdhury, Influence of spacing parameters on the wind loading of solar array, J. Fluids Struct. 48 (2014) 295–315, http://dx.doi.org/10.1016/j.jfluidstructs.2014.03.005.

[18] K. Strobel, D. Banks, Effects of vortex shedding in arrays of long inclined flat plates and ramifications for ground-mounted photovoltaic arrays, J. Wind Eng. Ind. Aerodyn. 133 (2014) 146–149, http://dx.doi.org/10.1016/j.jweia.2014.06.013.

[19] The American Society of Civil Engineers, Minimum Design Loads and Associated Criteria for Buildings and Other Structures, Technical Report, The American Society of Civil Engineers, Reston, VA, 2017, http://dx.doi.org/10.1061/9780784414248.

[20] G.T. Bitsuamlak, A.K. Dagnew, J. Erwin, Evaluation of wind loads on solar panel modules using CFD, in: Fifth International Symposium on Computational Wind Engineering, Chapel Hill, North Carolina, USA. May 23–27, 2010, URL: https://www.researchgate.net/publication/267263612.

[21] A.M. Aly, G. Bitsuamlak, Aerodynamics of ground-mounted solar panels: Test model scale effects, J. Wind Eng. Ind. Aerodyn. 123 (2013) 250–260, http://dx.doi.org/10.1016/j.jweia.2013.07.007.

[22] M. Shademan, R. Barron, R. Balachandar, H. Hangan, Numerical simulation of wind loading on ground-mounted solar panels at different flow configurations, Can. J. Civil Eng. 41 (2014) 728–738, http://dx.doi.org/10.1139/cjce-2013-0537.

[23] C.M. Jubayer, H. Hangan, Numerical simulation of wind effects on a stand-alone ground mounted photovoltaic (PV) system, J. Wind Eng. Ind. Aerodyn. 134 (2014) 56–64, http://dx.doi.org/10.1016/j.jweia.2014.08.008.

[24] C.M. Jubayer, H. Hangan, A numerical approach to the investigation of wind loading on an array of ground mounted solar photovoltaic (PV) panels, J. Wind Eng. Ind. Aerodyn. 153 (2016) 60–70, http://dx.doi.org/10.1016/j.jweia.2016.03.009.

[25] G.P. Reina, G.D. Stefano, Computational evaluation of wind loads on sun-tracking ground-mounted photovoltaic panel arrays, J. Wind Eng. Ind. Aerodyn. 170 (2017) 283–293, http://dx.doi.org/10.1016/j.jweia.2017.09.002.

[26] J. Holmes, Distribution of peak wind loads on a low-rise building, J. Wind Eng. Ind. Aerodyn. 29 (1–3) (1988) 59–67, http://dx.doi.org/10.1016/0167-6105(88)90145-6.

[27] A. Davenport, How can we simplify and generalize wind loads? J. Wind Eng. Ind. Aerodyn. 54–55 (C) (1995) 657–669, http://dx.doi.org/10.1016/0167-6105(94)00079-S.

[28] X. Chen, A. Kareem, Equivalent static wind loads for buffeting response of bridges, J. Struct. Eng. 127 (12) (2001) 1467–1475, http://dx.doi.org/10.1061/(ASCE)0733-9445(2001)127:12(1467).

[29] G. Frontini, T. Argentini, L. Rosa, D. Rocchi, Advances in the application of the principal static wind loads: A large-span roof case, Eng. Struct. 262 (2022) 114314, http://dx.doi.org/10.1016/j.engstruct.2022.114314.

[30] M. Browne, Z. Taylor, S. Li, S. Gamble, A wind load design method for ground-mounted multi-row solar arrays based on a compilation of wind tunnel experiments, J. Wind Eng. Ind. Aerodyn. 205 (2020) http://dx.doi.org/10.1016/j.jweia.2020.104294.

[31] E. Martínez-García, E. Blanco-Marigorta, J. Parrondo Gayo, A. Navarro-Manso, Influence of inertia and aspect ratio on the torsional galloping of single-axis solar trackers, Eng. Struct. 243 (2021) http://dx.doi.org/10.1016/j.engstruct.2021.112682.

[32] T. Bao, Z. Li, O. Pu, R.W. Chan, Z. Zhao, Y. Pan, Y. Yang, B. Huang, H. Wu, Modal analysis of tracking photovoltaic support system, Sol. Energy 265 (2023) 112088, http://dx.doi.org/10.1016/j.solener.2023.112088.

[33] D. Valentín, C. Valero, M. Egusquiza, A. Presas, Failure investigation of a solar tracker due to wind-induced torsional galloping, Eng. Fail. Anal. 135 (2022) 106137, http://dx.doi.org/10.1016/j.engfailanal.2022.106137.

[34] T. Guha, Y. Fewless, D. Banks, Effect of panel tilt, row spacing, ground clearance and post-offset distance on the vortex induced dynamic loads on fixed tilt ground mount photovoltaic arrays, in: 14th International Conference on Wind Engineering, 2015.

[35] Z.J. Taylor, M.A. Feero, M.T. Browne, Aeroelastic instability mechanisms of single-axis solar trackers, J. Wind Eng. Ind. Aerodyn. 244 (2024) 105626, http://dx.doi.org/10.1016/j.jweia.2023.105626.

[36] G. Diana, D. Rocchi, M. Belloli, Wind tunnel: a fundamental tool for long-span bridge design, Struct. Infrastruct. Eng. 11 (2015) 533–555, http://dx.doi.org/10.1080/15732479.2014.951860.

[37] J.A. Cárdenas-Rondón, M. Ogueta-Gutiérrez, S. Franchini, R. Manzanares-Bercial, Stability analysis of two-dimensional flat solar trackers using aerodynamic derivatives at different heights above ground, J. Wind Eng. Ind. Aerodyn. 243 (2023) 105606, http://dx.doi.org/10.1016/j.jweia.2023.105606.

[38] G. Diana, S. Stoyanoff, K. Aas-Jakobsen, A. Allsop, M. Andersen, T. Argentini, M.C. Montoya, S. Hernández, J.Á. Jurado, H. Katsuchi, I. Kavrakov, H.-K. Kim, G. Larose, A. Larsen, G. Morgenthal, O. Øiseth, S. Omarini, D. Rocchi, M. Svendsen, T. Wu, IABSE Task Group 3.1 Benchmark Results. Part 2: Numerical Analysis of a Three-Degree-of-Freedom Bridge Deck Section Based on Experimental Aerodynamics, Struct. Eng. Int. 30 (3) (2020) 411–420, http://dx.doi.org/10.1080/10168664.2019.1661331.

[39] G. Diana, S. Stoyanoff, K. Aas-Jakobsen, A. Allsop, M. Andersen, T. Argentini, M.C. Montoya, S. Hernández, J.Á. Jurado, H. Katsuchi, I. Kavrakov, H.-K. Kim, G. Larose, A. Larsen, G. Morgenthal, O. Øiseth, S. Omarini, D. Rocchi, M. Svendsen, T. Wu, IABSE Task Group 3.1 Benchmark Results. Part 1: Numerical Analysis of a

Two-Degree-of-Freedom Bridge Deck Section Based on Analytical Aerodynamics, Struct. Eng. Int. 30 (3) (2020) 401–410, http://dx.doi.org/10.1080/10168664.2019.1639480.

[40] A. Zasso, Flutter derivatives: Advantages of a new representation convention, J. Wind Eng. Ind. Aerodyn. 60 (1996) 35–47, http://dx.doi.org/10.1016/0167-6105(96)00022-0, The Wind Engineering Society's 2nd UK Conference.

[41] T. Argentini, A. Pagani, D. Rocchi, A. Zasso, Monte Carlo analysis of total damping and flutter speed of a long span bridge: Effects of structural and aerodynamic uncertainties, J. Wind Eng. Ind. Aerodyn. 128 (2014) 90–104, http://dx.doi.org/10.1016/j.jweia.2014.02.010.

[42] G. Frontini, T. Argentini, S. Muggiasca, M. Belloli, A framework for fatigue damage estimate in single-axis solar trackers, J. Phys. Conf. Ser. 2647 (2024) 242010, http://dx.doi.org/10.1088/1742-6596/2647/24/242010.

[43] A. Davenport, Note on the distribution of the largest value of a random function with application to gust loading, Proc. Inst. Civ. Eng. 28 (1964) 187–196, http://dx.doi.org/10.1680/iicep.1964.10112.

[44] D.K. Kwon, A. Kareem, Peak factors for non-Gaussian load effects revisited, J. Struct. Eng. 137 (2011) 1611–1619, http://dx.doi.org/10.1061/(ASCE)ST.1943-541X.0000412.

[45] N. Cook, The Designer's Guide to Wind Loading of Building Structures. Part 1, 1985, URL: https://www.scopus.com/inward/record.uri?eid=2-s2.0-85040859852&partnerID=40&md5=6762c9a928892a6b95905b24f7d7ef5d.

[46] E. Gumbel, Statistics of Extremes, Columbia University Press, 1958, http://dx.doi.org/10.7312/gumb92958.

[47] S.R. Ibrahim, E.C. Mikulcik, A method for the direct identification of vibration parameters from the free response, Shock. Vib. Bull. (1977) URL: https://api.semanticscholar.org/CorpusID:118998817.

[48] A.G. Chowdhury, P.P. Sarkar, A new technique for identification of eighteen flutter derivatives using a three-degree-of-freedom section model, Eng. Struct. 25 (2003) 1763–1772, http://dx.doi.org/10.1016/j.engstruct.2003.07.002.

[49] G. Bartoli, S. Contri, C. Mannini, M. Righi, Toward an improvement in the identification of bridge deck flutter derivatives, J. Eng. Mech. 135 (2009) 771–785, http://dx.doi.org/10.1061/(ASCE)0733-9399(2009)135:8(771).